Available online at www.sciencedirect.com

ScienceDirect

Energy Procedia 70 (2015) 182 – 192

Energy Procedia

International Conference on Solar Heating and Cooling for Buildings and Industry, SHC 2014

Coatings for heat storage reactors with hygroscopic salts

Ard-Jan de Jong[a]*, Ralph Stevens[b], Corné Rentrop[b], Christophe Hoegaerts[a]

[a]TNO, Van Mourik Broekmanweg 6, 2628 XE, Delft, The Netherlands
[b]TNO, De Rondom 1, 5612 AP, Eindhoven, The Netherlands

Abstract

One of the bottlenecks for realizing a commercial system for thermochemical heat storage using hygroscopic salts is corrosion induced by chemical side-reactions. E.g. when Na_2S hydrates are used, we basically deal with corrosion caused by the production of the volatile H_2S, threatening metal parts in the reactor and the vacuum system. Based on comparison with similar corrosion problems, epoxy coatings were selected to protect metal parts. Because of the complex geometry of the heat exchanger, e-coating was selected as application method. Applied coatings were tested by electrochemical impedance spectroscopy and by visual inspection. We found that flat areas were well covered, while defects were observed around edges and connections.

Peer-review by the scientific conference committee of SHC 2014 under responsibility of PSE AG

Keywords: thermochemical; energy storage; corrosion; coatings; electrochemical; impedance; spectroscopy; Kramers-Kronig transform

1. Introduction

Solar energy from an affordable area of commercial solar collectors would suffice for the yearly heat demand of a typical dwelling, provided that the excess heat from the warm season could be stored for later use during the cold season. Within the FP7 project MERITS, we cooperate on the development of a system for seasonal heat storage using hydration reactions of Na_2S, which can be reversed at practical solar collector temperatures of 80-90 °C for typical condenser temperatures. An overview of research questions at system, component and material level can be found in an earlier paper [1]. Presently, we study stabilization of the reactor and the connected vacuum system containing Na_2S. This involves stabilization of Na_2S itself in a suited composite thermochemical material (TCM),

* Corresponding author. Tel.: +31-(0)8886-64085; fax: +31-(0)8886-63023.
E-mail address: ardjan.dejong@tno.nl

Peer-review by the scientific conference committee of SHC 2014 under responsibility of PSE AG
doi:10.1016/j.egypro.2015.02.114

integrated with the heat exchanger (HX), but also the protection of metal interfaces in the reactor and the connected vacuum system against corrosion, induced by side-reactions of Na_2S. The present paper focuses on the latter issue. Our work consisted of two parts: coating selection and coating verification.

2. Coating selection

2.1. HX corrosion issues and solutions

The proposed HX is shown in Fig. 1a. It is based on standard air/liquid HXs, composed of a Copper (Cu) tube of ∅1cm inner diameter, going several times up and down through Aluminum (Al) fin plates. In total, the Cu-tubes crosses each Al-plate 12 times. During operation, the space between the fin plates is filled with TCM, allowing both the necessary vapor and heat transport towards the TCM, which is stabilized Na_2S for the MERITS reactor and test rig. The HX dimensions are 60×20×5 cm^3, with 4 mm fin spacing.

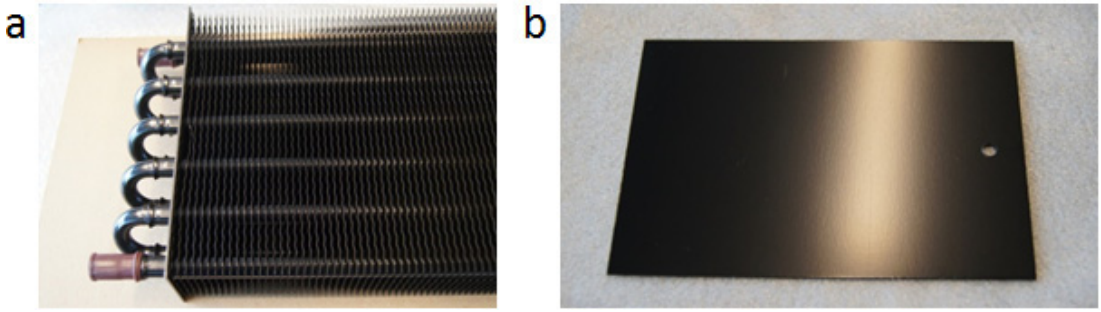

Fig. 1. (a) heat exchanger; (b) flat sample.

The HX materials Cu and Al are well-suited because of their good heat conductivities and affordability, but they are sensitive to corrosion. This can be induced by the following standard reactions at the Na_2S-stock:

$$Na_2S + H_2O \rightarrow 2Na^+ + S^{2-}$$
$$S^{2-} + H_2O \rightarrow HS^- + OH^-$$
$$HS^- + H_2O \rightarrow H_2S(g) + OH^-$$

Next, the volatile $H_2S(g)$ can spread through the vacuum system and dissolve in condensed water layers on any of the used construction metals Cu, Al or stainless steel. Here, the following corrosion reactions can take place:

$$H_2S + H_2O \rightarrow H^+ + HS^-$$
$$2H^+ + (2/n)Me \rightarrow H_2(g) + (2/n)Me^{n+}$$

Here, Me can be any of the construction metals. Problems caused by corrosion are degradation of construction materials, decay of the Na_2S stock and build-up of non-condensable gases (H_2S, H_2) that can block vapor transport at the evaporator/condenser and TCM interfaces. Several ways to solve this problem were considered:

- Use different construction materials, resistant to corrosion
- Apply a sufficiently noble metal coating
- Apply a resistant polymeric coating

The option of different construction materials is studied in another MERITS-task. Here, we will focus on protecting the above HX by application of a coating.

2.2. Coating trade-off

Coating the selected HX is challenging for several reasons. First, the coating must withstand Na_2S at operation temperatures between 20-80 °C in vacuum with about 12-42 mbar of water vapor. Due to the possibility of acid formation, the coating should be resistant to acid and strongly concentrated electrolytes. In addition, the coating must be robust to deformation when the HX is filled with TCM, and also withstand possible TCM volume changes during hydration and dehydration steps. Another challenge is application of the coating to the complex HX geometry, which includes complex forms with cavities as well as sharp edges.

Metal coatings are relatively expensive, especially metal coatings resistant to the given conditions. An obvious choice is epoxy coatings, because of their common usage in e.g. food and beverage cans (cf. [2]). The conditions in food and beverage cans are very similar to the above sketched conditions, with similarly acid and strongly concentrated electrolytes. When exposure to UV will occur, as for exterior car coatings, polyurethane (PUR) coatings are preferred, but these are somewhat more expensive. However, for cans and for our TCM reactors, UV is absent, as well as oxygen. Selecting epoxy as coating material, we next must select a method of coating application. Basic methods are (cf. [3]):

- Powder coating
- Spray coating
- Immersion coating
- Electrophoretic coating

The complex HX geometry makes powder and spray coating less attractive because of shadowing. Immersion coating is also not obvious, as filling the deep cavities between the fins by immersion without bridging requires a thin lacquer, making proper coating of the sharp fin edges more difficult. By electrophoretic coating (e-coating), an electric field is applied during immersion, attracting dissolved coating molecules particularly towards the sharper edges where the field is strongest. Thus, cavities as well as edges can be coated. E-coating is for instance commonly used for coating interior metal parts of cars. Our main considerations for choosing epoxy by e-coating are summarized in Table 1. Two different and independent suppliers were contacted for e-coating of the HXs of Fig. 1a as well as the flat samples of Fig. 1b.

Table 1. Coatings trade-off.

Coating	Method	Cu+Al	Geometry	Na_2S+H_2O	Deformation	Economy	Application
Ni, Cr	Electroplating			–	+	+/–	
Ni, Cr	Chemical			–	+	+/–	
Au, Pt	Electroplating			+	+	–	
Enamel					–		
PUR		+/–	+/–		+	+/–	Car exterior
Epoxy	Immersion		–	+	+	+	Cans
Epoxy	E-coat	+/–	+/–	+	+	+	Car interior

3. Coating verification

3.1. Introduction

The following coating verification methods were selected:

- Visual inspection, supported by microscope and endoscope
- Electric impedance spectroscopy (EIS)
- Long term exposure to Na_2S and H_2O vapor

Long term exposure studies are still being carried out at present. EIS is used for checking large coated areas on the presence of open defects such as pinholes and scratches (cf. [4]), and was carried out on flat samples as well as on entire HXs. Below, we describe how the EIS measurements were done and discuss the results, illustrated and supported by microscopic images.

3.2. EIS measurements

A common EIS setup is sketched in Fig. 2a, showing a coated substrate with a defect under immersion of electrolyte, which is contained in a cylinder mounted on the coating. In the electrolyte, a counter electrode (CE) is placed and the electric impedance Z is measured between the CE and the substrate or working electrode (WE).

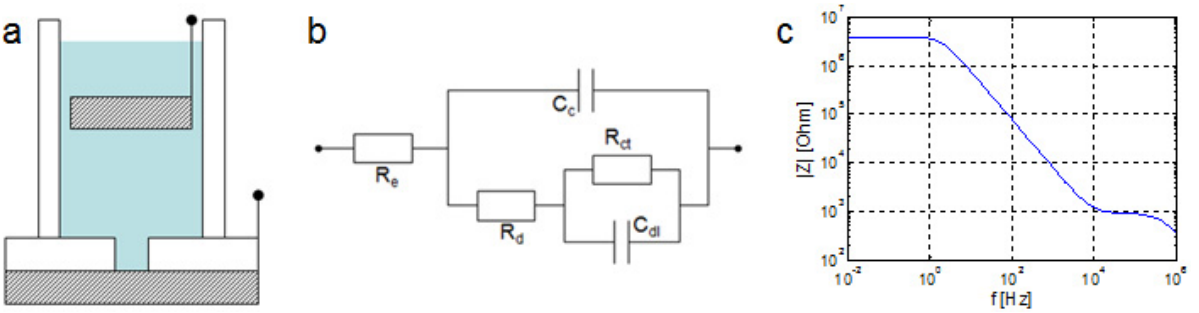

Fig. 2. (a) EIS setup; (b) Equivalent network; (c) Bode plot.

The electric impedance of an intact coating of area A and thickness L reads:

$$Z = \frac{1}{i\omega C_c} = \frac{L}{i\omega\varepsilon A} \tag{1}$$

Here, C_c is the coating capacity, $\omega = 2\pi f$, where f is the frequency and ε the coating permittivity. This impedance will be measured in the setup of Fig. 2a, with the addition of a small electrolyte resistance R_e. When the coating contains a defect, such as the pinhole in Fig. 2a, the equivalent EIS network will resemble Fig. 2b, with a parallel path containing a defect resistance, followed by the impedance of the double layer, which consists of a charge transfer resistance R_{ct} and a double layer capacitor C_{dl} (cf. [4]). The modulus $|Z|$ of the corresponding impedance spectrum for typical parameter values is shown in Fig. 2c. In particular, the DC impedance at $f = 0$ Hz reduces to the summation of the different resistors $R_{ct} + R_d + R_e$. For a sufficiently well conducting electrolyte, R_{ct} will usually be larger than R_d and R_e by several orders of magnitude (cf. [5]). In fact, one will generally choose an electrolyte with a sufficiently large conductivity so that for the given setup, the electrolyte can be regarded as one large electrode at an approximately fixed electric potential. Note that it takes more time to obtain the response at lower frequencies. E.g. for 10 mHz, a single cycle already takes 100 s. Provided that R_{ct} can be obtained from a recorded spectrum, one can estimate the total defect area A_{ct} in the immersed coating area A by:

$$R_{ct} = \frac{r_{ct}}{A_{ct}} \tag{2}$$

Here, the specific charge transfer resistance r_{ct} is determined by the speed of the chemical reaction transferring the electron current in the electrodes to an ion current in the electrolyte. Thus, from a measurement of R_{ct}, we obtain the defect area via $A_{ct} = r_{ct}/R_{ct}$. For that, we first estimate r_{ct} from a measurement on an artificial defect of known size (cf. [5]). The smallest defect area that can be detected is related to the lowest frequency of the spectrum. This follows from the consideration that the largest time constant will be $\tau_{max} = R_{ct}C_c$, so that arriving at the plateau $|Z| = R_{ct}$ requires a spectrum extending to $\omega_{min} = 1/R_{ct}C_c$. Conversely, when using a spectrum with $\omega > \omega_{min}$, the maximum value of R_{ct} that can be measured reads $R_{ct,max} = 1/\omega_{min}C_c$. Substitution of (1) and (2) implies that the minimum value of the defect area A_{ct} that can be detected is given by $A_{ct,min}/A = \omega_{min}\varepsilon r_{ct}/L$. Hence for a given coating, the smallest defects can be measured for a small immersed area A, a small ω_{min}, and rapid charge transfer.

3.3. Flat samples – flat coated area testing and checking for stray capacities

First we studied flat coated samples to check if the e-coating on flat areas is intact. Besides, by varying the immersion area A and checking the corresponding impedance change, we verified if our setup really measurers the immersed coating impedance, with negligible contribution of stray capacities. The following EIS settings were found satisfactory:

- Spectrum from 0.1 Hz to 100 kHz
- Amplitude 100 mV
- 10 s per cycle for all frequencies

We used an IviumStat impedance analyzer with a ∅5 mm Carbon electrode as CE, shown in Fig. 3a. A separate reference electrode (RE) was not used, because the voltage drop over the large CE area will be negligible compared to the voltage drop over the much smaller defect area. As electrolyte we used 1 M H_2SO_4, having a conductivity of about 8.4 S/m [6]. The electrolyte resistance is then in the order of $R_e = L_e/\sigma A_e \cong 12\ \Omega$ taking $L_e \cong 1$ cm and $A_e = 1\ cm^2$. This R_e is negligible compared to the impedances that we will measure. Besides, the selected electrolyte will rapidly dissolve a possibly present oxide layer in the defect, and provides the necessary well-defined charge transfer from electrons to ions and vice versa by the reaction $2H^+ + 2e^- \leftrightarrow H_2$ at the electrode interfaces.

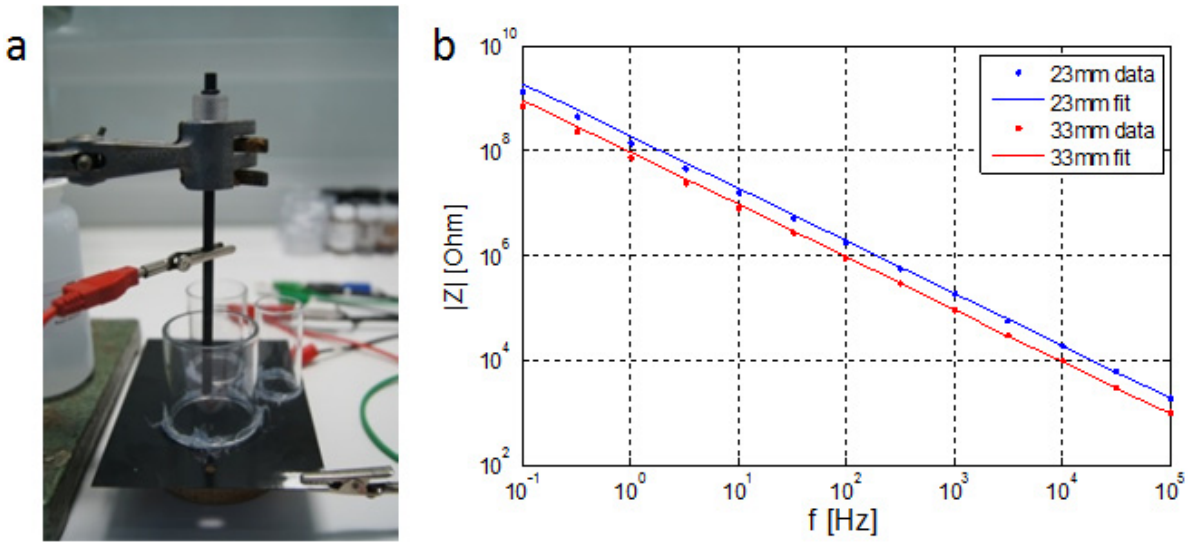

Fig. 3. (a) EIS setup for flat samples, different cylinder diameters; (b) EIS results.

Fig. 3b shows measurements on flat samples using two different cylinders of ∅23 mm and ∅33 mm, where dots are data and lines are fitted data. First we note that the spectra show a $1/f$ response conform a perfect capacitor, implying that the coating on the flat sample is intact. The blue line is a fit with $\varepsilon = 3.0\times10^{-11}$ F/m and $L = 15$ µm. The resulting coating capacity $C = 831$ pF for the small cylinder scales with the area to 1711 pF for the large cylinder. With the latter capacity value, the red line is computed, which corresponds rather well with the data. This implies that we really measure the immersed coating impedance with negligible influence of stray capacities.

3.4. Flat samples – artificial defect calibration

For the estimation of defect area from coating impedance by (2), we first need to estimate r_{ct} for Aluminum in 1 M H_2SO_4. For that, we measured the impedance spectrum of an artificial defect of known size, shown in Fig. 4a.

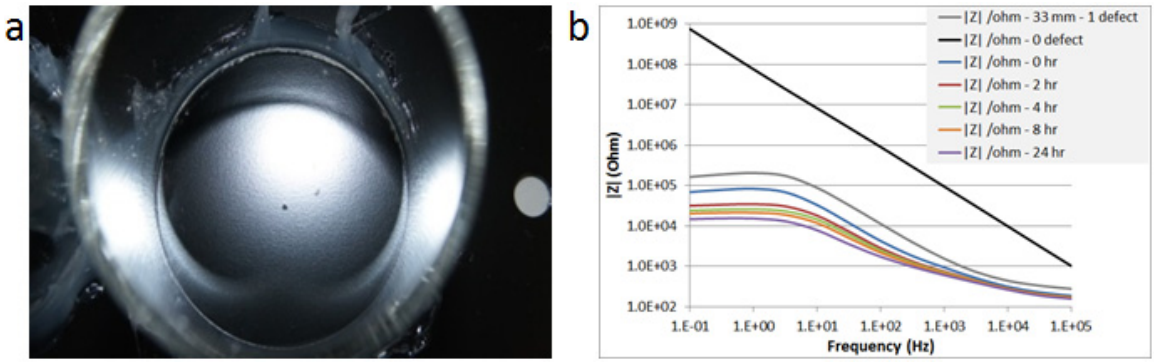

Fig. 4. (a) sample with artificial defect; (b) EIS results.

The corresponding spectra of Fig. 4b are recorded during 24 hours, and show gradually decreasing R_{ct}. This can be due to dissolution of an oxide layer or an air bubble in the defect, or by an increasing delamination area. Besides, the coating capacity C_c may increase due to water uptake, which may be used for studying water transport in coatings (cf. [5, 7]). The punctured defect was about ∅700 µm, corresponding to an area of $A_{ct} = 3.8\times10^{-7}$ m^2. With $R_{ct} = 30$ kΩ, we arrive at an estimation of $r_{ct} = R_{ct}A_{ct} = 0.0115$ Ωm^2 for the specific charge transfer resistance. This value will be further used below for the estimation of defect areas.

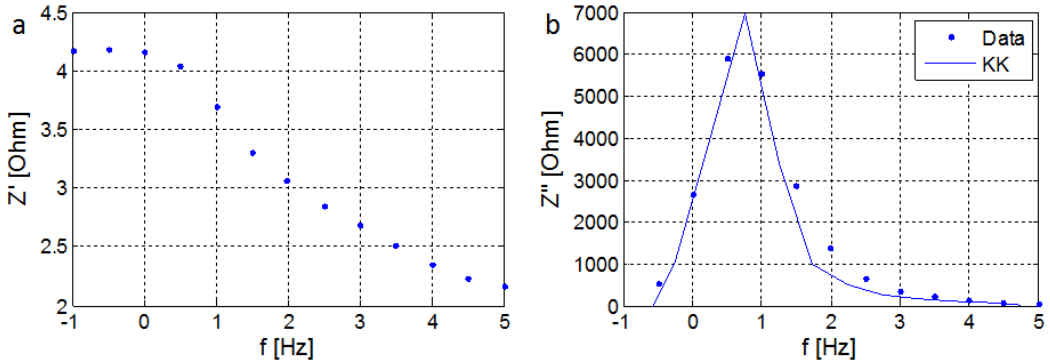

Fig. 5. (a) real part Z' from data; (b) imaginary part Z'' from data and from Kramers-Kronig transform of Z'.

For time-dependent measurements, one needs to check if the system can be regarded as linear, causal and time-invariant. In that case, the real and imaginary parts Z' and Z'' of the impedance $Z \equiv Z' - iZ''$ are related by the Kramers-Kronig transforms (cf. [4, 8]), providing an additional data validation check. Estimation of these transforms is discussed in Appendix A. Fig. 5a and b show the results for artificial defects during exposure, where dots are measured data. The solid curve in Fig. 5b is obtained by the Kramers-Kronig transform. Due to the rather large frequency spacing of 2 points per decade, the result is not very smooth, but corresponds rather well with the data.

3.5. Flat samples – edge coverage

We measured the edges of flat coated samples to verify if the e-coating procedure was also able to cover sharp edges. For that, we immersed the edge of a flat sample in electrolyte together with the CE, as shown in Fig. 5a. The blank area connected to the WE is also visible. The sample is 19.5 cm wide and immersed by 4 cm. The red curve of Fig. 5b shows that the edges are defect with about $R_{ct} = 1$ MΩ. This corresponds to a defect area of about $A_{ct} = r_{ct}/R_{ct} = 1.15\times10^{-8}$ m^2 = 0.0115 mm^2. To verify if the observed defects are really on the edges, the edges were covered with tape. This indeed increased R_{ct} to about 10 MΩ, implying that the tape had reduced the defect area by nearly a factor 10. This supports the hypothesis that on flat samples, defects are basically located around edges.

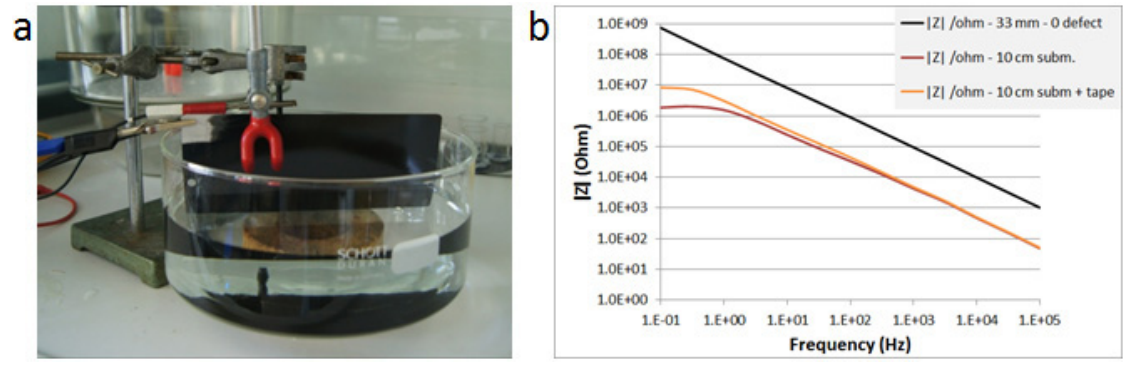

Fig. 6. (a) EIS setup for flat sample edges; (b) EIS results with and without tape.

3.6. Heat exchanger

Coating testing for an entire HX might be done by randomly selecting a few examples of a large batch of HXs, dismount some of the fin plates and test them for corrosion in the small setup of Fig. 2a. Non-destructive testing requires immersion of the entire HX in a sufficiently large tank filled with electrolyte, as shown in Fig. 7a. Also visible is a larger enveloping containment, used for safety reasons.

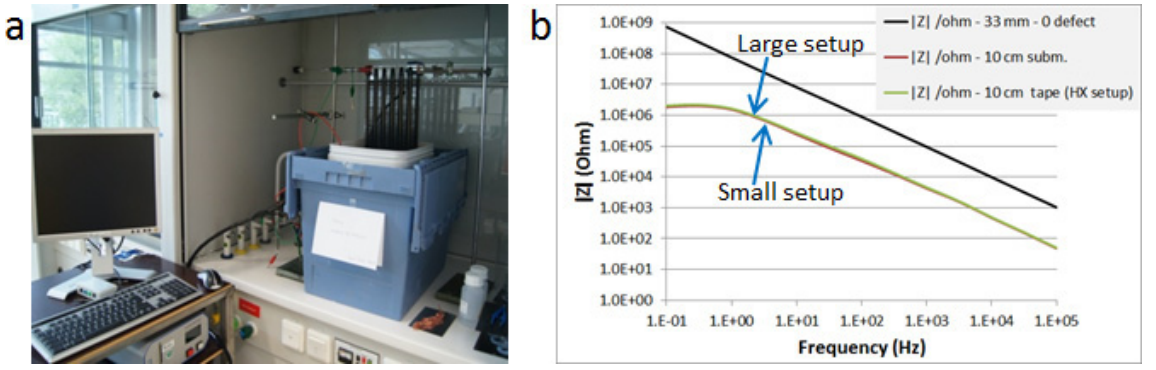

Fig. 7. (a) Large EIS setup for an entire HX; (b) EIS results flat sample, vertically immersed in small and large setups.

First, we repeated the EIS measurement of the flat sample edges in the large setup to check the large setup for stray capacities. The green curve in Fig. 7a shows the spectrum in the large setup, which indeed corresponds to the red curve that was earlier recorded in the small setup.

The large setup allows detection of defects along the height of the HX by gradually increasing the electrolyte level, as illustrated by Fig. 8a. Corresponding EIS results are shown in Fig. 8b. With only the Cu-tubes immersed, we obtained the orange curve, which is not parallel to perfect capacitor behavior, but neither we reach a clear plateau at the lowest frequencies. The red and blue lines shows immersion to the first and second fin plates. Estimating R_{ct} = 10 MΩ for the Cu-tubes and 300 Ω and 100 Ω for immersion up to the first and second fin plates, we obtain defect areas of 0.00115 mm^2 for the Cu-tubes, 38 mm^2 for the first and 115 mm^2 for the first plus second fin plates.

The observed charge transfer resistances are smaller than we expected from our earlier EIS measurements on edge defects. For the experiment of Fig. 6, we observed R_{ct} = 1 MΩ for 19.5 + 2×4 = 27.5 cm of immersed edge. For a single fin plate, we have 2×20 + 2×5 = 50 cm of edges. By scaling, we predict R_{ct} = 0.55 MΩ, much larger than the observed 300 Ω for immersion up to the first fin plate. Similarly, for immersion up to two fin plates, we predict 0.275 MΩ, again much larger than the observed 100 Ω. This suggests that for the entire HX, edge defects are not the dominant contribution and we have to look for another suspect. This may be the connections between Cu-tubes and Al-plates. Here, the lacquer has to penetrate the rectangular connection, which also has to be properly cleaned.

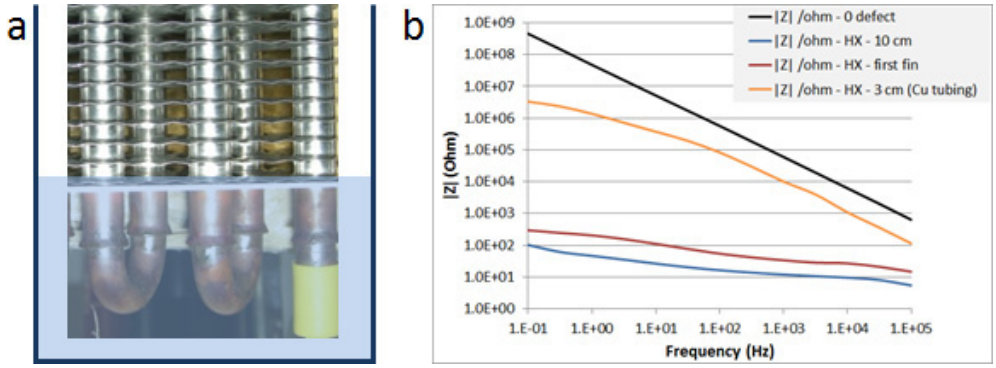

Fig. 8. (a) HX partially immersed in the large setup; (b) EIS results.

Visual inspection was carried out to locate the defects. The HX was taken apart and Fig. 9a shows an optical microscope image of fin edges, where defects appear as bubbles. This suggests that these defects originate from the formation of H_2-bubbles during the e-coating process. This may happen during pretreatment by acids, or during electrophoresis, when the substrate is the cathode. The latter would explain why especially edges are prone to defects, as the electric field will be strongest near edges. From the Cu-Al interface, stereo microscopy images were taken, as shown in Fig. 9b. The red arrows indicate what seems to be a sequence of defects and some line defects showing bare copper. Estimating a defect width of 0.1 mm, the total defect area of 115 mm^2 of the first and second fin suggests 115 cm of defects. With 12 Cu-tubes crossing each Al-plate, this amounts to 115/24 = 4.8 cm of defects per connection. This is of the same order as the tube circumference, so the observed charge transfer resistance may indeed be due to defects at Cu-Al connections.

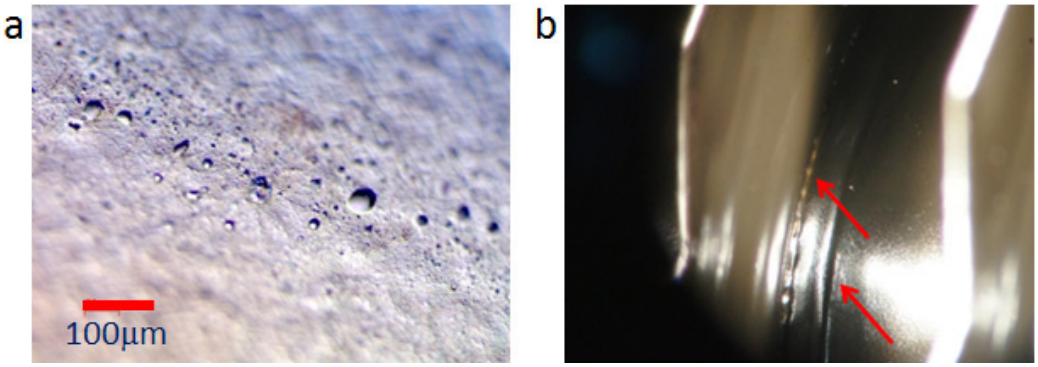

Fig. 9. (a) Fin edge defects; (b) Cu-Al connection defects.

4. Conclusions and follow-up

Small and large setups were implemented for EIS measurements on flat samples and on the entire HX. Several validity checks on the setup were carried out successfully. By scaling of the immersion area, we checked for stray capacities. Causality and time-invariance were checked by Kramers-Kronig transforms. The large setup for the entire HX was checked by measuring one and the same sample in both the small and large setups.

E-coating works well for the flat parts of the samples. Defects were found around the edges of flat samples as well as around the edges of fin plates taken from the entire HX. By optical microscopy, the defects show up as bubbles, which suggests that the defects are due to H_2 formation during the e-coating process. However, the defect area for the entire HX estimated by EIS was much larger than expected from edge defects only. For the entire HX, the major part of the defect area is probably due to defects at the connections between Cu-tubes and Al-plates, for which visual inspection by a stereo microscope indeed shows areas with the appearance of bare copper.

A following step will be exposure experiments of coated samples and the entire HX under typical operational conditions, i.e. with a layer of Na_2S on the coating, 12-42 mbar of H_2O vapor and temperatures between 20-80 °C. If necessary, we will study several ways of coating repair by dedicated lacquers, and we will study and optimize coating application. Finally, different HX materials with better corrosion resistance may be considered, such as Titanium or even polymers, provided that they can be made sufficiently impermeable to water vapor. Due to smaller specific heat conductivity, different construction materials may also require a different type of HX.

Acknowledgements

The research leading to these results has received funding from the European Commission Seventh Framework Programme (FP/2007-2013) under grant agreement No ENER/FP7/295983 (MERITS). MERITS is a R&D project supported by the European FP7 program with the aim to build a prototype of a compact rechargeable thermal battery. Such a product would offer a new solution for improved use of renewable sources for domestic heating, cooling and hot water appliances and thus greatly contribute to the European ambition of an energy-neutral built environment by 2050.

The project is carried out by four research institutes (TNO, VITO, Tecnalia, Fraunhofer ISE), two universities (Ulster University, University of Lleida), two SME's (De Beijer RTB, Zonne-Energie Nederland BV), and two industries (Mostostal, Glen Dimplex). The team will work with novel high energy density thermochemical materials that can supply required heating, cooling and domestic hot water for a dwelling with up to 100% renewable energy sources (e.g. the sun) throughout the year. The key development issues are:

- The delivery of heat on different dedicated temperature levels for heating, cooling and domestic hot water
- The tailoring to the requirements of individual dwellings
- The design and development of a dedicated solar collector
- The integrated design for the components and enhanced thermo-chemical materials, including the control system

Furthermore the project includes the development of business models and market strategies to foster market take-up before 2020. More information on MERITS is available on our public website "www.MERITS.eu".

Appendix A. Numerical evaluation of the Kramers-Kronig transforms

The complex impedance $Z(\omega) \equiv Z'(\omega) - iZ''(\omega)$, with real and imaginary parts $Z'(\omega)$ and $Z''(\omega)$, can be expressed by the following integral transform (cf. [9]):

$$Z(\omega) = \int_{\tau=0}^{\infty} \frac{f(\tau)d\tau}{1+i\omega\tau} = \int_{\tau=0}^{\infty} \frac{1}{1+(\omega\tau)^2} f(\tau)d\tau - i\int_{\tau=0}^{\infty} \frac{\omega\tau}{1+(\omega\tau)^2} f(\tau)d\tau \equiv Z'(\omega) - iZ''(\omega) \quad \text{(A.1)}$$

This can be regarded as a continuous summation over relaxations with time constant τ and amplitude $f(\tau)d\tau$. Thus, $f(\tau)$ can be regarded as a time constant distribution, with peaks at time constants τ_1, τ_2 and so on corresponding to break point frequencies f_1, f_2 and so on of characteristic processes in the studied system. Time constants may include a time constant $\tau = RC$ of a resistor R and capacitor C, or the time constant of a dipole relaxation, e.g. of a water molecule in liquid water, or the time constant of a dipole in a polymer. Equation (A.1) suggests that $f(\tau)$ can be obtained from either $Z'(\omega)$ and $Z''(\omega)$. This provides a route for relating $Z'(\omega)$ and $Z''(\omega)$ and finding a relation similar to the Kramers-Kronig transforms [5]. We briefly summarize the derivation here. With the substitution $f(\tau)d\tau = \tau f(\tau)\tau^{-1}d\tau = \tau f(\tau)d\ln\tau \equiv g(-\ln\tau)d\ln\tau$, we obtain:

$$Z(\omega) = \int_{\ln\tau=-\infty}^{\infty} \frac{g(-\ln\tau)d\ln\tau}{1+i\omega\tau} \quad \text{(A.2)}$$

Next, with the substitutions $p \equiv \ln\omega$, $q \equiv -\ln\tau$, $y(p) \equiv Z(\omega)$, we obtain:

$$y(p) = \int_{q=\infty}^{-\infty} \frac{-g(q)dq}{1+ie^{p-q}} = \int_{q=-\infty}^{\infty} \frac{g(q)dq}{1+ie^{p-q}} \equiv y'(p) - iy''(p) \tag{A.3}$$

For the real and imaginary parts, one can explicitly write:

$$\begin{aligned} y'(p) &= \int_{q=-\infty}^{\infty} \frac{1}{1+e^{2(p-q)}} g(q)dq \equiv \int_{q=-\infty}^{\infty} h'(p-q)g(q)dq \\ y''(p) &= \int_{q=-\infty}^{\infty} \frac{e^{p-q}}{1+e^{2(p-q)}} g(q)dq \equiv \int_{q=-\infty}^{\infty} h''(p-q)g(q)dq \end{aligned} \tag{A.4}$$

These substitutions are a common idea for rewriting integral equations with a product kernel such as (A.2) into the form of convolution integrals, for instance used by Gardner [10] for obtaining $f(\tau)$ from time domain data instead of frequency domain data $Z(\omega)$. We first deal with the lower integral of (A.4), introducing the Fourier transforms $Y''(k)$, $H''(k)$ and $G(k)$ of $y''(p)$, $h''(p)$ and $g(p)$ respectively, according to the following common definition:

$$G(k) \equiv \int_{p=-\infty}^{\infty} e^{-ikp} g(p)dp \tag{A.5}$$

Similarly, the Fourier transforms $Y''(k)$ and $H''(k)$ are obtained from $y''(p)$ and $h''(p)$. In the k-space, the second convolution integral of (A.4) reduces to the following product:

$$Y''(k) = H''(k)G(k) \tag{A.6}$$

One application of (A.6) is obtaining the time constant distribution $f(\tau)$ from a sufficiently complete measurement of $Z''(\omega)$. This can be done by first computing $Y''(k)$ from $Z''(\omega)$, then obtain $G(k) = Y''(k)/H''(k)$, and finally by $\tau f(\tau) = g(-\ln\tau) = g(q)$ via Fourier inversion of $G(k)$. Here one can use an explicit expression for $H''(k)$, which can be obtained from the observation that $h''(p) = 1/2\cosh(p)$ and the following identity:

$$H''(k) = F_k\left\{\frac{1}{2\cosh(p)}\right\} = \frac{\pi/2}{\cosh(\pi k/2)} \tag{A.7}$$

Note that for actual data containing noise, one will need low-pass filtering prior to the inversion, as the kernel $1/H''(k)$ for obtaining $G(k)$ from $Y''(k)$ does not vanish, but even diverges for $|k| \to \infty$. One would like to follow a similar approach for obtaining $f(\tau)$ from $Z'(\omega)$, but the Fourier transform of $h'(p)$ does not converge. One way out is working with dy'/dp instead of $y'(p)$ by differentiation of the first convolution integral of (A.4):

$$\frac{dy'}{dp} = -\int_{q=-\infty}^{\infty} \frac{1}{2\cosh^2[2(p-q)]} g(q)dq \tag{A.8}$$

The Fourier transform of the kernel of this convolution integral can also be written in closed form:

$$F_k\left\{\frac{1}{2\cosh^2(2p)}\right\} = \frac{\pi k/2}{\sinh(\pi k/2)} \tag{A.9}$$

We now have two expressions for estimating $f(\tau)$, one using the real and one using the imaginary part of the impedance $Z(\omega)$ [5]:

$$\begin{aligned} G(k) &= \frac{\sinh(\pi k/2)}{\pi k/2} F_k\left\{-\frac{dy'}{dp}\right\} \\ G(k) &= \frac{\cosh(\pi k/2)}{\pi/2} F_k\{y''(p)\} \end{aligned} \tag{A.10}$$

This completes the inversion. In addition, as the left hand sides of these equations are equal, we obtain [5]:

$$F_k\{y''(p)\} = \frac{\tanh(\pi k/2)}{k} F_k\left\{-\frac{dy'}{dp}\right\} \tag{A.11}$$

This identity allows determination of the real part $Z'(\omega)$ from the imaginary part $Z''(\omega)$ and vice versa. Thus, formula (A.11) is equivalent and in fact an alternative formulation of the Kramers-Kronig transforms. Note that (A.11) allows numerical evaluation of the transform with nothing more than Fourier transforms and estimation of the derivative $dZ'/dp = dZ'(\omega)/d\ln\omega$. Thus, one avoids the practical issues of evaluating an integral with a pole on the interval, which is needed when the classical formulation of the Kramers-Kronig transforms is used (cf. [8]), or the evaluation of an integral with a 0/0 division on the interval when using Macdonald's formulation [4]. These issues may be particularly tricky when carrying out the Kramers-Kronig transforms for measured actual data including noise. We add that besides these practical issues, formulas (A.10) and (A.11) may also be of theoretical value.

Finally we note that for $k \cong 0$, we have $\tanh(\pi k/2) \cong \pi k/2$, so that for $k \to 0$, the kernel of (A.11) allows analytic continuation by $\tanh(\pi k/2)/k \to \pi/2$. This also implies that for smooth functions $y'(p)$ and $y''(p)$, for which small k-values are most important, one can replace the kernel by $\pi/2$. This leads to the following approximation:

$$y''(p) \cong -\frac{\pi}{2}\frac{dy'}{dp} \tag{A.12}$$

In terms of the impedance, this expression reads:

$$Z''(\omega) \cong -\frac{\pi}{2}\frac{dZ'}{d\ln\omega} \tag{A.13}$$

Thus, the well-known Staverman-Schwarzl approximation (cf. [9]) is obtained in a natural way. Finally, we note that the kernel $\tanh(\pi k/2)/k$ of (A.11) vanishes for $|k| \to \infty$, and thus already acts as a low pass filter, suppressing noise when obtaining $Z''(\omega)$ from $Z'(\omega)$. For data with high noise level, the inversion may require additional low pass filtering. The latter will also be necessary when (A.11) is used for obtaining $Z'(\omega)$ from $Z''(\omega)$, in which case the kernel $k/\tanh(\pi k/2)$ does not vanish for $|k| \to \infty$.

References

[1] De Jong AJ, Trausel F, Finck C, Van Vliet L, Cuypers R. Energy Procedia 2014;48:309-19.
[2] Montenari A, Pezzani A, Cassarà A, Quantara A, Lupi R. Progress in Organic Coatings 1996;29:159-65.
[3] Doorgeest T, De Jong RI. Handboek bedrijfsvoering industrieel coaten; 1998.
[4] Macdonald JR. Impedance Spectroscopy; 1987.
[5] De Jong, AJ. Characterization of Coatings Inside Food and Beverage Cans. PhD thesis, Delft; 2000.
[6] Busenberg E. Water-Resources Investigations Report 87-4060; 1987.
[7] Van Westing EPM. Determination of Coating Performance with Impedance Measurements, Delft; 1992.
[8] Sakurai JJ. Advanced Quantum Mechanics; 1967.
[9] Böttcher CJF, Bordewijk P. Theory of Electric Polarization; 1978.
[10] Gardner DG, Gardner JC, Meinke WW. J Chem Phys 1959;31:978-86.